



Modeling optimizes PEM fuel cell durability using three-dimensional multi-phase computational fluid dynamics model

Maher A.R. Sadiq Al-Baghdadi

Fuel Cell Research Center, International Energy & Environment Foundation, Al-Najaf, P.O.Box 39, Iraq.

Abstract

Damage mechanisms in a proton exchange membrane (PEM) fuel cell are accelerated by mechanical stresses arising during fuel cell assembly (bolt assembling), and the stresses arise during fuel cell running, because it consists of the materials with different thermal expansion and swelling coefficients. Therefore, in order to acquire a complete understanding of the damage mechanisms in the membrane and gas diffusion layers, mechanical response under steady-state hygro-thermal stresses should be studied under real cell operating conditions and in real cell geometry (three-dimensional).

In this work, full three-dimensional, non-isothermal computational fluid dynamics model of a PEM fuel cell has been developed to simulate the hygro and thermal stresses in PEM fuel cell, which are occurring during the cell operation due to the changes of temperature and relative humidity. A unique feature of the present model is to incorporate the effect of hygro and thermal stresses into actual three-dimensional fuel cell model. The mechanical behaviour of the membrane, catalyst layers, and gas diffusion layers during the operation of a unit cell has been studied and investigated. The model is shown to be able to understand the many interacting, complex electrochemical, transport phenomena, and stresses distribution that have limited experimental data. The results show that the non-uniform distribution of stresses, caused by the temperature gradient in the cell, induces localized bending stresses, which can contribute to delaminating between the membrane and the gas diffusion layers. These results may explain the occurrence of cracks and pinholes in the membrane during regular cell operation. This model is used to study the effect of operating, design, and material parameters on fuel cell hygro-thermal stresses in polymer membrane, catalyst layers, and gas diffusion layers. Detailed analyses of the fuel cell durability under various operating conditions have been conducted and examined. The analysis helped identifying critical parameters and shed insight into the physical mechanisms leading to a fuel cell durability under various operating conditions.

Optimization study of a PEM fuel cell durability has been performed. To achieve long cell life, the results show that the cell must be operate at lower cell operating temperature, higher cell operating pressure, higher stoichiometric flow ratio, and must have higher GDL porosity, higher GDL thermal conductivity, higher membrane thermal conductivity, narrower gases channels, thicker gas diffusion layers, and thinner membrane. In these optimum conditions, the maximum deformation (displacement) reduction by about 50% than the base case operating conditions.

Copyright © 2010 International Energy and Environment Foundation - All rights reserved.

Keywords: PEM, Durability, Hygro-thermal stress, CFD, Modelling.

1. Introduction

Durability is one of the most critical remaining issues impeding successful commercialization of broad PEM fuel cell stationary and transportation energy applications, and the durability of fuel cell stack components remains, in most cases, insufficiently understood. Lengthy required testing times, lack of understanding of most degradation mechanisms, and the difficulty of performing in-situ, non-destructive structural evaluation of key components makes the topic a difficult one [1, 2].

The Membrane-Electrode-Assembly (MEA) is the core component of PEM fuel cell and consists of membrane with the gas-diffusion layers including the catalyst attached to each side. The fuel cell MEA durability plays a vital role in the overall lifetime achieved by a stack in field applications. Within the MEA's electrocatalyst layers are three critical interfaces that must remain properly intermingled for optimum MEA performance: platinum/carbon interface (for electron transport and catalyst support); platinum/Nafion interface (for proton transport); and Nafion/carbon interface (for high-activity catalyst dispersion and structural integrity). The MEA performance shows degradation over operating time, which is dependent upon materials, fabrication and operating conditions [3, 4].

Durability is a complicated phenomenon; linked to the chemical and mechanical interactions of the fuel cell components, i.e. electro-catalysts, membranes, gas diffusion layers, and bipolar plates, under severe environmental conditions, such as elevated temperature and low humidity [5]. In fuel cell systems, failure may occur in several ways such as chemical degradation of the ionomer membrane or mechanical failure in the PEM that results in gradual reduction of ionic conductivity, increase in the total cell resistance, and the reduction of voltage and loss of output power [6]. Mechanical degradation is often the cause of early life failures. Mechanical damage in the PEM can appear as through-the-thickness flaws or pinholes in the membrane, or delaminating between the polymer membrane and gas diffusion layers [7, 8].

Mechanical stresses which limit MEA durability have two origins. Firstly, this is the stresses arising during fuel cell assembly (bolt assembling). The bolts provide the tightness and the electrical conductivity between the contact elements. Secondly, additional mechanical stresses occur during fuel cell running because PEM fuel cell components have different thermal expansion and swelling coefficients. Thermal and humidity gradients in the fuel cell produce dilatations obstructed by tightening of the screw-bolts. Compressive stress increasing with the hygro-thermal loading can exceed the yield strength which causes the plastic deformation. The mechanical behaviour of the membrane depends strongly on hydration and temperature [9, 10].

Water management is one of the critical operation issues in proton exchange membrane (PEM) fuel cells. Spatially varying concentrations of water in both vapour and liquid form are expected throughout the cell because of varying rates of production and transport. Devising better water management is therefore a key issue in PEM fuel cell design, and this requires improved understanding of the parameters affecting water transport in the membrane [11, 12]. Thermal management is also required to remove the heat produced by the electrochemical reaction in order to prevent drying out of the membrane, which in turn can result not only in reduced performance but also in eventual rupture of the membrane [13, 14]. Thermal management is also essential for the control of the water evaporation or condensation rates [15]. As a result of in the changes in temperature and moisture, the PEM, gas diffusion layers (GDL), and bipolar plates will all experience expansion and contraction. Because of the different thermal expansion and swelling coefficients between these materials, hygro-thermal stresses are expected to be introduced into the unit cell during operation. In addition, the non-uniform current and reactant flow distributions in the cell can result in non-uniform temperature and moisture content of the cell, which could in turn, potentially causing localized increases in the stress magnitudes. The need for improved lifetime of PEM fuel cells necessitates that the failure mechanisms be clearly understood and life prediction models be developed, so that new designs can be introduced to improve long-term performance. Increasing of the durability is a significant challenge for the development of fuel cell technology. Membrane failure is believed to be the result of combined chemical and mechanical effects acting together [1, 2, 5]. Variations in temperature and humidity during operation cause stresses and strains (mechanical loading) in the membrane as well as the MEA and is considered to be the mechanical failure driving force in fuel cell applications [6-10]. Reactant gas cross over, hydrogen peroxide formation and movement, and cationic contaminants are all to be major factors contributing to the chemical decomposition of polymer electrolyte membranes. While chemical degradation of membranes has been investigated and reported extensively in literature [1-8], there has been little work published on mechanical degradation of the membrane. Investigating the mechanical response of the membrane subjected to change in humidity and

temperature requires studying and modelling of the stress-strain behaviour of membranes and MEAs. Weber and Newman [16] developed one-dimensional model to study the stresses development in the fuel cell. They showed that hygro-thermal stresses might be an important reason for membrane failure, and the mechanical stresses might be particularly important in systems that are non-isothermal. However, their model is one-dimensional and does not include the effects of material property mismatch among PEM, GDL, and bipolar plates.

Tang et al. [17] studied the hygro and thermal stresses in the fuel cell caused by step-changes of temperature and relative humidity. Influence of membrane thickness was also studied, which shows a less significant effect. However, their model is two-dimensional, where the hygro-thermal stresses are absent in the third direction (flow direction). In addition, a simplified temperature and humidity profile with no internal heat generation were assumed, (constant temperature for each upper and lower surfaces of the membrane was assumed).

Kusoglu et al. [18] developed two-dimensional model to investigate the mechanical response of a PEM subjected to a single hygro-thermal loading cycle, simulating a simplified single fuel cell duty cycle. A linear, uncoupled, simplified temperature and humidity profile with no internal heat generation, assuming steady-state conditions, was used for the loading and unloading conditions. Linear-elastic, perfectly plastic material response with temperature and humidity dependent material properties was used to study the plastic deformation behaviour of the membrane during the cycle. The stress evolution during a simplified operating cycle is determined for two alignments of the bipolar plates. They showed that the alternating gas channel alignment produces higher shear stresses than the aligned gas channel. Their results suggested that the in-plane residual tensile stresses after one fuel cell duty cycle developed upon unloading, may lead to the failure of the membranes due to the mechanical fatigue. They concluded that in order to acquire a complete understanding of these damage mechanisms in the membranes, mechanical response under continuous hygro-thermal cycles should be studied under realistic cell operating conditions.

Kusoglu et al. [19] investigated the mechanical response of proton exchange membranes in a fuel cell assembly under humidity cycles at a constant temperature. The behaviour of the membrane under hydration and dehydration cycles was simulated by imposing a simplified humidity gradient profile from the cathode to the anode. Also, a simplified temperature profile with no internal heat generation were assumed. Linear elastic, plastic constitutive behaviour with isotropic hardening and temperature and humidity dependent material properties were utilized in the simulations for the membrane. The evolution of the stresses and plastic deformation during the humidity cycles were determined using two-dimensional finite elements model for various levels of swelling anisotropy. They showed that the membrane response strongly depends on the swelling anisotropy where the stress amplitude decreases with increasing anisotropy. Their results suggested that it may be possible to optimize a membrane with respect to swelling anisotropy to achieve better fatigue resistance, potentially enhancing the durability of fuel cell membranes.

Solasi et al. [20] developed two-dimensional model to define and understand the basic mechanical behaviour of ionomeric membranes clamped in a rigid frame, and subjected to changes in temperature and humidification. Expansion/contraction mechanical response of the constrained membrane as a result of change in hydration and temperature was also studied in non-uniform geometry. A circular hole in the centre of the membrane can represent pinhole creation or even material degradation during fuel cell operation was considered as the extreme form of non-uniformity in this constraint configuration. Their results showed that the hydration have a bigger effect than temperature in developing mechanical stresses in the membrane. These stresses will be more critical when non-uniformity as a form of hydration profile or a physical pinhole exists across the membrane.

Bogachev et al. [21] developed a linear elastic-plastic two-dimensional model of fuel cell with hardening for analysis of mechanical stresses in MEA arising in cell assembly procedure. The model includes the main components of real fuel cell (membrane, gas diffusion layers, graphite plates, and seal joints) and clamping elements (steel plates, bolts, nuts). The stress and plastic deformation in MEA are simulated taking into account the realistic clamping conditions. Their results concluded that important variations of stresses generated during the assembling procedure can be a source of the limitation of the mechanical reliability of the system.

Suvorov et al. [22] analyzed the stress relaxation in the membrane electrode assemblies (MEA) in PEM fuel cells subjected to compressive loads using numerical simulations (finite element method). This behaviour is important because nonzero contact stress is required to maintain low electric resistivity in

the fuel cell stack. In addition to the two-dimensional assumption, the temperature was kept fixed and equal to the operating temperature at all time. All properties were considered to be independent of the temperature. They showed that under applied compressive strains the contact stress in the membrane electrode assembly (MEA) will drop with time. The maximum contact stress and the rate of stress relaxation depend on the individual properties of the membrane and the gas diffusion layer.

Tang et al. [23] examined the hygro-thermo-mechanical properties and response of a class of reinforced hydrated perfluorosulfonic acid membranes (PFSA) in a fuel cell assembly under humidity cycles at a constant temperature. The load imposed keeps the membrane at elevated temperature (85 C) and linearly cycles the relative humidity between the initial (30% RH) and the hydrated state (95% RH) at the cathode side of membrane. The evolution of hygro-thermally induced mechanical stresses during the load cycles were determined for reinforced and unreinforced PFSA membranes using two-dimensional finite elements model. Their numerical simulations showed that the in-plane stresses for reinforced PFSA membrane remain compressive during the cycling. Compressive stresses are advantageous with respect to fatigue loading, since compressive in-plane stresses will significantly reduce the slow crack growth associated with fatigue failures. They showed that the reinforced PFSA membrane exhibits higher strength and lower in-plane swelling than the unreinforced PFSA membrane used as a reference, therefore, should result in higher fuel cell durability.

Bogachev et al. [24] developed two-dimensional model to study the evolution of stresses and plastic deformations in the membrane during the turn-on phase. They showed that the maximal stresses in the membrane take place during the humidification step before the temperature comes to its steady-state value. The magnitude of these stresses is sufficient for initiation of the plastic deformations in the Nafion membrane. The plastic deformations in the membrane develop during the entire humidification step. At the steady state the stresses have the highest value in the centre of the membrane; the Mises stress is equal to 2.5 MPa.

In addition to the two-dimensional assumption, the operating conditions have been taken into account by imposing the heating sources as a simplified directly related relationship between power generation and efficiency of the fuel cell. The moisture is set gradually from an initial value of 35% up to 100%. The humidity is imposed after all heat sources reach steady state. The imposed moisture is assumed to be uniformly distributed in the membrane during turn-on stage (before reaching the steady state). However, this questionable assumption leads to overestimation of the maximal stresses in the membrane during turn-on stage.

Al-Baghdadi and Shahad [25] incorporated the effect of hygro and thermal stresses into non-isothermal three-dimensional CFD model of PEM fuel cell to simulate the hygro and thermal stresses in one part of the fuel cell components, which is the polymer membrane. They studied the behaviour of the membrane during the operation of a unit cell. The results showed that the displacement have the highest value in the centre of the membrane near the cathode side inlet area.

An operating fuel cell has varying local conditions of temperature, humidity, and power generation (and thereby heat generation) across the active area of the fuel cell in three-dimensions. Nevertheless, except of ref. [25], no models have yet been published to incorporate the effect of hygro-thermal stresses into actual fuel cell models to study the effect of these real conditions on the stresses developed in membrane and gas diffusion layers. In addition, as a result of the architecture of a cell, the transport phenomena in a fuel cell are inherently three-dimensional, but no models have yet been published to address the hygro-thermal stresses in PEM fuel cells with three-dimensional effect. Suvorov et al. [22] reported that the error introduced due to two-dimensional assumption is about 10%. Therefore, in order to acquire a complete understanding of the damage mechanisms in the membrane and gas diffusion layers, mechanical response under steady-state hygro-thermal stresses should be studied under real cell operating conditions and in real cell geometry (three-dimensional).

The difficult experimental environment of fuel cell systems has stimulated efforts to develop models that could simulate and predict multi-dimensional coupled transport of reactants, heat and charged species using computational fluid dynamic (CFD) methods. A comprehensive computational model should include the equations and other numerical relations needed to fully define fuel cell behaviour over the range of interest. In the present work, full three-dimensional, non-isothermal computational fluid dynamics model of a PEM fuel cell has been developed to simulate the hygro and thermal stresses in PEM fuel cell, which are occurring during the cell operation due to the changes of temperature and relative humidity. This model is used to study the effect of operating, design, and material parameters on fuel cell performance and hygro-thermal stresses in the fuel cell MEA.

2. Model description

The present work presents a comprehensive three-dimensional, multi-phase, non-isothermal model of a PEM fuel cell that incorporates the significant physical processes and the key parameters affecting fuel cell performance. The model accounts for both gas and liquid phase in the same computational domain, and thus allows for the implementation of phase change inside the gas diffusion layers. The model includes the transport of gaseous species, liquid water, protons, and energy. Water transport inside the porous gas diffusion layer and catalyst layer is described by two physical mechanisms: viscous drag and capillary pressure forces, and is described by advection within the gas channels. Water transport across the membrane is also described by two physical mechanisms: electro-osmotic drag and diffusion. The model features an algorithm that allows for a more realistic representation of the local activation overpotentials, which leads to improved prediction of the local current density distribution. This leads to high accuracy prediction of temperature distribution in the cell and therefore thermal stresses. This model also takes into account convection and diffusion of different species in the channels as well as in the porous gas diffusion layer, heat transfer in the solids as well as in the gases, and electrochemical reactions. The present multi-phase model is capable of identifying important parameters for the wetting behaviour of the gas diffusion layers and can be used to identify conditions that might lead to the onset of pore plugging, which has a detrimental effect of the fuel cell performance. A unique feature of the model is to incorporate the effect of hygro-thermal stresses into actual three-dimensional fuel cell model. This model is used to investigate the hygro and thermal stresses in PEM fuel cell, which developed during the cell operation due to the changes of temperature and relative humidity.

2.1 Computational domain

A computational model of an entire cell would require very large computing resources and excessively long simulation times. The computational domain in this study is therefore limited to one straight flow channel with the land areas. The full computational domain consists of cathode and anode gas flow channels, and the membrane electrode assembly as shown in Figure 1.

2.2 Model equations

2.2.1 Gas flow channels

In the fuel cell channels, the gas-flow field is obtained by solving the steady-state Navier-Stokes equations, i.e. the continuity equation, the mass conservation equation for each phase yields the volume fraction (r) and along with the momentum equations the pressure distribution inside the channels. The continuity equation for the gas phase inside the channel is given by;

$$\nabla \cdot (r_g \rho_g \mathbf{u}_g) = 0 \quad (1)$$

and for the liquid phase inside the channel becomes;

$$\nabla \cdot (r_l \rho_l \mathbf{u}_l) = 0 \quad (2)$$

where \mathbf{u} is velocity vector [m/s], ρ is density [kg/m³].

Two sets of momentum equations are solved in the channels, and they share the same pressure field. Under these conditions, it can be shown that the momentum equations becomes;

$$\nabla \cdot (\rho_g \mathbf{u}_g \otimes \mathbf{u}_g - \mu_g \nabla \mathbf{u}_g) = -\nabla r_g \left(P + \frac{2}{3} \mu_g \nabla \cdot \mathbf{u}_g \right) + \nabla \cdot [\mu_g (\nabla \mathbf{u}_g)^T] \quad (3)$$

$$\nabla \cdot (\rho_l \mathbf{u}_l \otimes \mathbf{u}_l - \mu_l \nabla \mathbf{u}_l) = -\nabla r_l \left(P + \frac{2}{3} \mu_l \nabla \cdot \mathbf{u}_l \right) + \nabla \cdot [\mu_l (\nabla \mathbf{u}_l)^T] \quad (4)$$

where P is pressure (Pa), μ is viscosity [kg/(m·s)].

The mass balance is described by the divergence of the mass flux through diffusion and convection. Multiple species are considered in the gas phase only, and the species conservation equation in multi-component, multi-phase flow can be written in the following expression for species i ;

$$\nabla \cdot \left[-r_g \rho_g y_i \sum_{j=1}^N D_{ij} \frac{M}{M_j} \left[\left(\nabla y_j + y_j \frac{\nabla M}{M} \right) + (x_j - y_j) \frac{\nabla P}{P} \right] + r_g \rho_g y_i \cdot \mathbf{u}_g + D_i^T \frac{\nabla T}{T} \right] = 0 \quad (5)$$

where T is temperature (K), y is mass fraction, x is mole fraction, D is diffusion coefficient [m²/s]. Subscript i denotes oxygen at the cathode side and hydrogen at the anode side, and j is water vapour in both cases. Nitrogen is the third species at the cathode side.

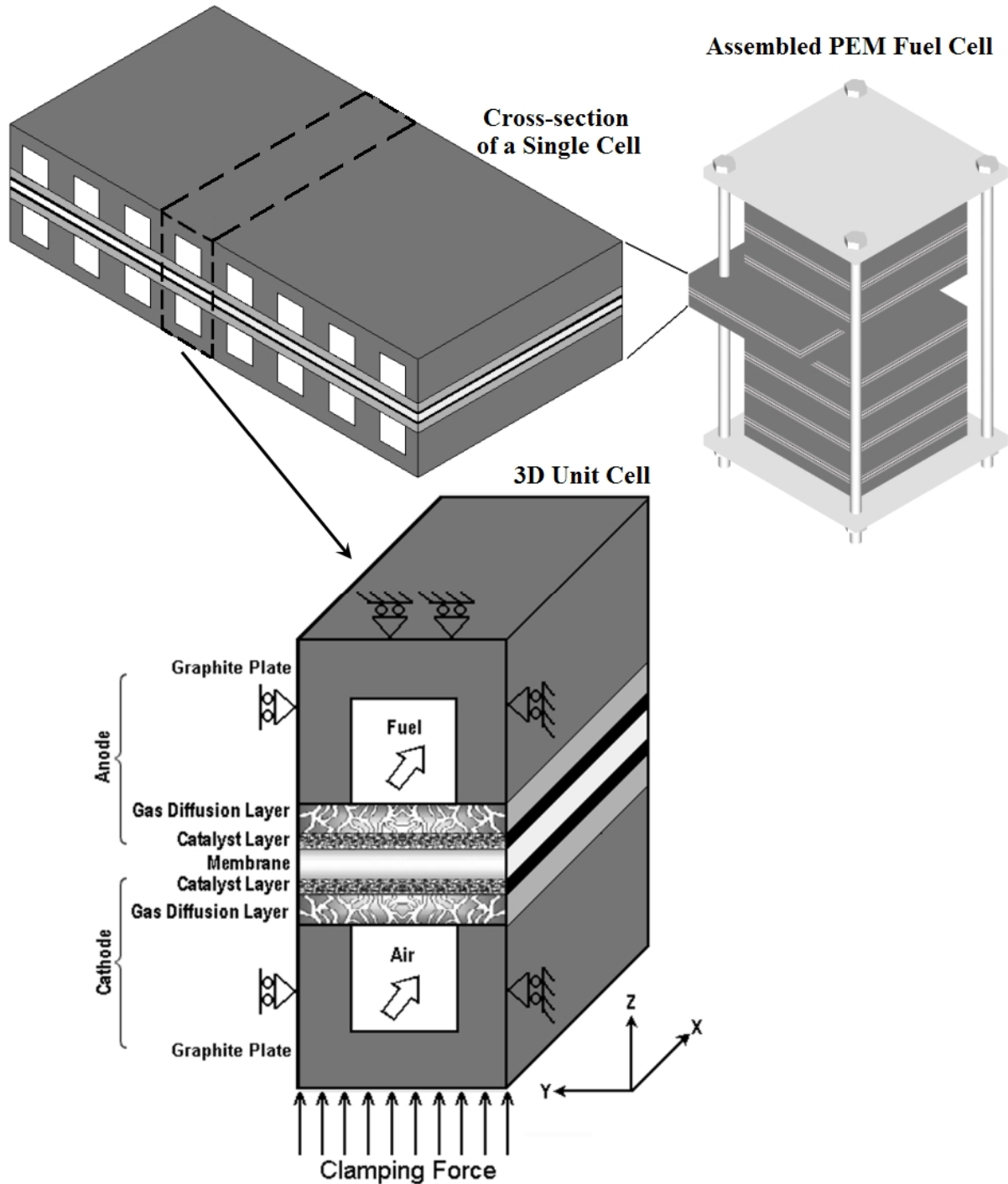


Figure 1. Three-dimensional computational domain

The Maxwell-Stefan diffusion coefficients of any two species are dependent on temperature and pressure. They can be calculated according to the empirical relation based on kinetic gas theory [8];

$$D_{ij} = \frac{T^{1.75} \times 10^{-3}}{P \left[\left(\sum_k V_{ki} \right)^{1/3} + \left(\sum_k V_{kj} \right)^{1/3} \right]^2} \left[\frac{1}{M_i} + \frac{1}{M_j} \right]^{1/2} \quad (6)$$

In this equation, the pressure is in atm and the binary diffusion coefficient D_{ij} is in $[\text{cm}^2/\text{s}]$. The values for $\left(\sum V_{ki} \right)$ are given by Fuller et al. [8].

The temperature field is obtained by solving the convective energy equation;

$$\nabla \cdot (r_g (\rho_g C_p \mathbf{u}_g T - k_g \nabla T)) = 0 \quad (7)$$

where C_p is specific heat capacity $[\text{J}/(\text{kg} \cdot \text{K})]$, k is gas thermal conductivity $[\text{W}/(\text{m} \cdot \text{K})]$.

The gas phase and the liquid phase are assumed to be in thermodynamic equilibrium; hence, the temperature of the liquid water is the same as the gas phase temperature.

2.2.2 Gas diffusion layers

The physics of multiple phases through a porous medium is further complicated here with phase change and the sources and sinks associated with the electrochemical reaction. The equations used to describe transport in the gas diffusion layers are given below. Mass transfer in the form of evaporation ($\dot{m}_{phase} > 0$) and condensation ($\dot{m}_{phase} < 0$) is assumed, so that the mass balance equations for both phases are;

$$\nabla \cdot ((1 - sat) \rho_g \varepsilon \mathbf{u}_g) = \dot{m}_{phase} \quad (8)$$

$$\nabla \cdot (sat \cdot \rho_l \varepsilon \mathbf{u}_l) = \dot{m}_{phase} \quad (9)$$

where sat is saturation, ε is porosity

The momentum equation for the gas phase reduces to Darcy's law, which is, however, based on the relative permeability for the gas phase (KP). The relative permeability accounts for the reduction in pore space available for one phase due to the existence of the second phase [9].

The momentum equation for the gas phase inside the gas diffusion layer becomes;

$$\mathbf{u}_g = -(1 - sat) KP \nabla P / \mu_g \quad (10)$$

where KP is hydraulic permeability $[\text{m}^2]$.

Two liquid water transport mechanisms are considered; shear, which drags the liquid phase along with the gas phase in the direction of the pressure gradient, and capillary forces, which drive liquid water from high to low saturation regions [9]. Therefore, the momentum equation for the liquid phase inside the gas diffusion layer becomes;

$$\mathbf{u}_l = -\frac{KP_l}{\mu_l} \nabla P + \frac{KP_l}{\mu_l} \frac{\partial P_c}{\partial sat} \nabla sat \quad (11)$$

where P_c is capillary pressure $[\text{Pa}]$.

The functional variation of capillary pressure with saturation is prescribed following Leverett [9] who has shown that;

$$P_c = \tau \left(\frac{\varepsilon}{KP} \right)^{1/2} \left(1.417(1 - sat) - 2.12(1 - sat)^2 + 1.263(1 - sat)^3 \right) \quad (12)$$

where τ is surface tension $[\text{N}/\text{m}]$.

The liquid phase consists of pure water, while the gas phase has multi components. The transport of each species in the gas phase is governed by a general convection-diffusion equation in conjunction which the Stefan-Maxwell equations to account for multi species diffusion;

$$\nabla \cdot \left[-(1-sat)\rho_g \varepsilon y_i \sum_{j=1}^N D_{ij} \frac{M}{M_j} \left[\left(\nabla y_j + y_j \frac{\nabla M}{M} \right) + (x_j - y_j) \frac{\nabla P}{P} \right] + (1-sat)\rho_g \varepsilon y_i \cdot \mathbf{u}_g + \varepsilon D_i^T \frac{\nabla T}{T} \right] = \dot{m}_{phase} \quad (13)$$

In order to account for geometric constraints of the porous media, the diffusivities are corrected using the Bruggemann correction formula [10];

$$D_{ij}^{eff} = D_{ij} \times \varepsilon^{1.5} \quad (14)$$

The heat transfer in the gas diffusion layers is governed by the energy equation as follows;

$$\nabla \cdot \left((1-sat) \left(\rho_g \varepsilon C_{p_g} \mathbf{u}_g T - k_{eff,g} \varepsilon \nabla T \right) \right) = \varepsilon \beta (T_{solid} - T) - \varepsilon \dot{m}_{phase} \Delta H_{evap} \quad (15)$$

where k_{eff} is effective electrode thermal conductivity [W/(m·K)]; the term $[\varepsilon \beta (T_{solid} - T)]$, on the right hand side, accounts for the heat exchange to and from the solid matrix of the GDL. The gas phase and the liquid phase are assumed to be in thermodynamic equilibrium, i.e., the liquid water and the gas phase are at the same temperature.

The potential distribution in the gas diffusion layers is governed by;

$$\nabla \cdot (\lambda_e \nabla \phi) = 0 \quad (16)$$

where λ_e is electrode electronic conductivity [S/m].

In order to account for the magnitude of phase change inside the GDL, expressions are required to relate the level of over- and undersaturation as well as the amount of liquid water present to the amount of water undergoing phase change. In the present work, the procedure of Berning and Djilali [9] was used to account for the magnitude of phase change inside the GDL.

2.2.3 Catalyst layers

The catalyst layer is treated as a thin interface, where sink and source terms for the reactants are implemented. Due to the infinitesimal thickness, the source terms are actually implemented in the last grid cell of the porous medium. At the cathode side, the sink term for oxygen is given by;

$$S_{O_2} = -\frac{M_{O_2}}{4F} i_c \quad (17)$$

where F is Faraday's constant (96487 [C/mole]), i_c is cathode local current density [A/m²], M is molecular weight [kg/mole].

Whereas the sink term for hydrogen is specified as;

$$S_{H_2} = -\frac{M_{H_2}}{2F} i_a \quad (18)$$

where i_a is anode local current density [A/m²]

The production of water is modelled as a source terms, and hence can be written as;

$$S_{H_2O} = \frac{M_{H_2O}}{2F} i_c \quad (19)$$

The generation of heat in the cell is due to entropy changes as well as irreversibility's due to the activation overpotential [11];

$$\dot{q} = \left[\frac{T(-\Delta s)}{n_e F} + \eta_{act} \right] i \quad (20)$$

where \dot{q} is heat generation [W/m²], n_e is number of electrons transfer, s is specific entropy [J/(mole.K)], η_{act} is activation overpotential (V).

The local current density distribution in the catalyst layers is modelled by the Butler-Volmer equation [12], [13];

$$i_c = i_{o,c}^{ref} \left(\frac{C_{O_2}}{C_{O_2}^{ref}} \right) \left[\exp\left(\frac{\alpha_a F}{RT} \eta_{act,c} \right) + \exp\left(-\frac{\alpha_c F}{RT} \eta_{act,c} \right) \right] \quad (21)$$

$$i_a = i_{o,a}^{ref} \left(\frac{C_{H_2}}{C_{H_2}^{ref}} \right)^{1/2} \left[\exp\left(\frac{\alpha_a F}{RT} \eta_{act,a} \right) + \exp\left(-\frac{\alpha_c F}{RT} \eta_{act,a} \right) \right] \quad (22)$$

where C_{H_2} is local hydrogen concentration [mole/m³], $C_{H_2}^{ref}$ is reference hydrogen concentration [mole/m³], C_{O_2} is local oxygen concentration [mole/m³], $C_{O_2}^{ref}$ is reference oxygen concentration [mole/m³], $i_{o,a}^{ref}$ is anode reference exchange current density, $i_{o,c}^{ref}$ is cathode reference exchange current density, R is universal gas constant (8.314 [J/(mole·K)]), α_a is charge transfer coefficient, anode side, and α_c is charge transfer coefficient, cathode side.

2.2.4 Membrane

The balance between the electro-osmotic drag of water from anode to cathode and back diffusion from cathode to anode yields the net water flux through the membrane;

$$N_w = n_d M_{H_2O} \frac{i}{F} - \nabla \cdot (\rho D_w \nabla c_w) \quad (23)$$

where N_w is net water flux across the membrane [kg/(m²·s)], n_d is electro-osmotic drag coefficient. The water diffusivity in the polymer can be calculated as follow [14];

$$D_w = 1.3 \times 10^{-10} \exp \left[2416 \left(\frac{1}{303} - \frac{1}{T} \right) \right] \quad (24)$$

The variable c_w represents the number of water molecules per sulfonic acid group (i.e. mol H_2O /equivalent SO_3^-). The water content in the electrolyte phase is related to water vapour activity via [15], [16];

$$\begin{aligned} c_w &= 0.043 + 17.81a - 39.85a^2 + 36.0a^3 & (0 < a \leq 1) \\ c_w &= 14.0 + 1.4(a - 1) & (1 < a \leq 3) \\ c_w &= 16.8 & (a \geq 3) \end{aligned} \quad (25)$$

The water vapour activity a given by;

$$a = x_w P / P_{sat} \quad (26)$$

Heat transfer in the membrane is governed by;

$$\nabla \cdot (k_{mem} \cdot \nabla T) = 0 \quad (27)$$

where k_{mem} is membrane thermal conductivity [W/(m·K)].

The potential loss in the membrane is due to resistance to proton transport across membrane, and is governed by;

$$\nabla \cdot (\lambda_m \nabla \phi) = 0 \quad (28)$$

where λ_m is membrane ionic conductivity [S/m].

2.2.5 Hygro-Thermal stresses in fuel cell

Using hygrothermoelasticity theory, the effects of temperature and moisture as well as the mechanical forces on the behaviour of elastic bodies have been addressed. An uncoupled theory is assumed, for which the additional temperature changes brought by the strain are neglected [2]. The total strain tensor is determined using the following expression;

$$\pi = \pi_M + \pi_T + \pi_S \quad (29)$$

where, π_M is the contribution from the mechanical forces and π_T , π_S are the thermal and swelling induced strains, respectively.

The thermal strains resulting from a change in temperature of an unconstrained isotropic volume are given by;

$$\pi_T = \wp(T - T_{Ref}) \quad (30)$$

where \wp is thermal expansion [1/K].

The swelling strains caused by moisture change in membrane are given by;

$$\pi_S = \lambda_{mem}(\mathfrak{R} - \mathfrak{R}_{Ref}) \quad (31)$$

where λ_{mem} is membrane humidity swelling-expansion tensor and \mathfrak{R} is the relative humidity [%].

Assuming linear response within the elastic region, the isotropic Hooke's law is used to determine the stress tensor σ .

$$\sigma = \mathbf{G}\pi \quad (32)$$

where \mathbf{G} is the constitutive matrix.

The effective stresses according to von Mises, 'Mises stresses', are given by;

$$\sigma_v = \sqrt{\frac{(\sigma_1 - \sigma_2)^2 + (\sigma_2 - \sigma_3)^2 + (\sigma_3 - \sigma_1)^2}{2}} \quad (33)$$

where σ_1 , σ_2 , σ_3 are the principal stresses.

The mechanical boundary conditions are noted in Figure 1. The initial conditions corresponding to zero stress-state are defined; all components of the cell stack are set to reference temperature 20 C, and relative humidity 35% (corresponding to the assembly conditions) [17, 24, 35]. In addition, a constant pressure of (1 MPa) is applied on the surface of lower graphite plate, corresponding to a case where the fuel cell stack is equipped with springs to control the clamping force [17-19, 21, 24].

2.3 Computational procedure

The governing equations were discretized using a finite-volume method and solved using the multi-physics CFD code. Stringent numerical tests were performed to ensure that the solutions were independent of the grid size. A computational quadratic mesh consisting of a total of 64586 nodes and 350143 meshes was found to provide sufficient spatial resolution (Figure 2). The coupled set of equations was solved iteratively, and the solution was considered to be convergent when the relative error was less than 1.0×10^{-6} in each field between two consecutive iterations. The calculations presented here have all been obtained on a Pentium IV PC (3 GHz, 2 GB RAM), using Windows XP operating system.

The geometric and the base case operating conditions are listed in Table 1. The values of the electrochemical transport parameters for the base case operating conditions are listed in Table 2. The material properties used in this model are also listed in Table 2.

The solution begins by specifying a desired current density of the cell to use for calculating the inlet flowrates at the anode and cathode sides. An initial guess of the activation overpotential is obtained from the desired current density using the Butler–Volmer equation. Then follows by computing the flow fields for each phase for velocities u , v , w , and pressure P . Once the flow field is obtained, the mass fraction equations are solved for the mass fractions of oxygen, hydrogen, nitrogen, and water. Scalar equations are solved last in the sequence of the transport equations for the temperature field in the cell and potential fields in the gas diffusion layers and the membrane. The local current densities are solved based on the Butler–Volmer equation. After the local current densities are obtained, the local activation overpotentials can be readily calculated from the Butler–Volmer equation. The local activation overpotentials are updated after each global iterative loop. Hooke's law with total strain tensor is solved to determine the

stress tensor. Convergence criteria are then performed on each variable and the procedure is repeated until convergence. The properties are updated after each global iterative loop based on the new local gas composition and temperature. Source terms reflect changes in the overall gas phase mass flow due to consumption or production of gas species via reaction and due to mass transfer between water in the vapour phase and water that is in the liquid phase (phase-change). The flow diagram of the algorithm is shown in Figure 3.

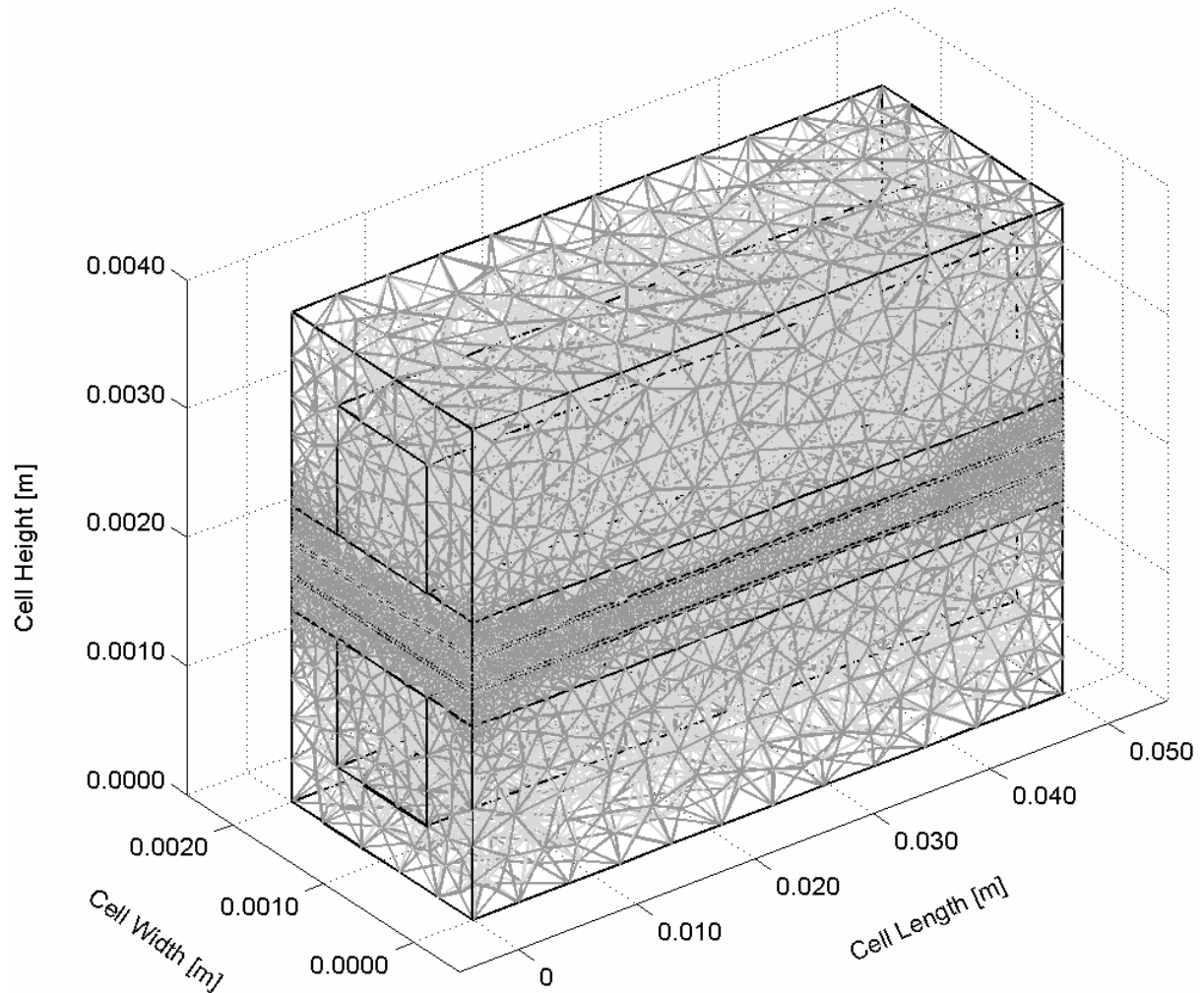


Figure 2. Computational mesh of a PEM fuel cell

Table 1. Geometrical and operational parameters for base case conditions

| Parameter | Symbol | Value | Unit |
|-----------------------------------------------------------------------|-----------------|--------------|-------------|
| Channel length | L | 0.05 | m |
| Channel width | W | 1e-3 | m |
| Channel height | H | 1e-3 | m |
| Land area width | W_{land} | 1e-3 | m |
| Gas diffusion layer thickness | δ_{GDL} | 0.26e-3 | m |
| Wet membrane thickness (Nafion® 117) | δ_{mem} | 0.23e-3 | m |
| Catalyst layer thickness | δ_{CL} | 0.0287e-3 | m |
| Hydrogen reference mole fraction | $x_{H_2}^{ref}$ | 0.84639 | - |
| Oxygen reference mole fraction | $x_{O_2}^{ref}$ | 0.17774 | - |
| Anode pressure | P_a | 3 | atm |
| Cathode pressure | P_c | 3 | atm |
| Inlet fuel and air temperature | T_{cell} | 353.15 | K |
| Relative humidity of inlet fuel and air (fully humidified conditions) | Ψ | 100 | % |
| Air stoichiometric flow ratio | ξ_c | 2 | - |
| Fuel stoichiometric flow ratio | ξ_a | 2 | - |

Table 2. Electrode and membrane parameters for base case operating conditions

| Parameter | Symbol | Value | Unit | Ref. |
|-------------------------------------------------------|-------------------------|-----------|------------|------|
| Electrode porosity | ε | 0.4 | - | [13] |
| Electrode electronic conductivity | λ_e | 100 | S/m | [15] |
| Membrane ionic conductivity (Nafion [®] 117) | λ_m | 17.1223 | S/m | [28] |
| Transfer coefficient, anode side | α_a | 0.5 | - | [13] |
| Transfer coefficient, cathode side | α_c | 1 | - | [32] |
| Cathode reference exchange current density | $i_{o,c}^{ref}$ | 1.8081e-3 | A/m^2 | [14] |
| Anode reference exchange current density | $i_{o,a}^{ref}$ | 2465.598 | A/m^2 | [14] |
| Electrode thermal conductivity | k_{eff} | 1.3 | $W/m.K$ | [28] |
| Membrane thermal conductivity | k_{mem} | 0.455 | $W/m.K$ | [28] |
| Electrode hydraulic permeability | kp | 1.76e-11 | m^2 | [31] |
| Entropy change of cathode side reaction | ΔS | -326.36 | $J/mole.K$ | [30] |
| Heat transfer coefficient between solid and gas phase | β | 4e6 | W/m^3 | [13] |
| Protonic diffusion coefficient | D_{H^+} | 4.5e-9 | m^2/s | [13] |
| Fixed-charge concentration | c_f | 1200 | $mole/m^3$ | [13] |
| Fixed-site charge | z_f | -1 | - | [13] |
| Electro-osmotic drag coefficient | n_d | 2.5 | - | [28] |
| Electrode Poisson's ratio | \mathfrak{S}_{GDL} | 0.25 | - | [17] |
| Membrane Poisson's ratio | \mathfrak{S}_{mem} | 0.25 | - | [17] |
| Electrode thermal expansion | \wp_{GDL} | -0.8e-6 | $1/K$ | [17] |
| Membrane thermal expansion | \wp_{mem} | 123e-6 | $1/K$ | [35] |
| Electrode Young's modulus | Ψ_{GDL} | 1e10 | Pa | [17] |
| Membrane Young's modulus | Ψ_{mem} | 249e6 | Pa | [35] |
| Electrode density | ρ_{GDL} | 400 | kg/m^3 | [17] |
| Membrane density | ρ_{mem} | 2000 | kg/m^3 | [17] |
| Membrane humidity swelling-expansion tensor | $\tilde{\lambda}_{mem}$ | 23e-4 | $1/\%$ | [17] |

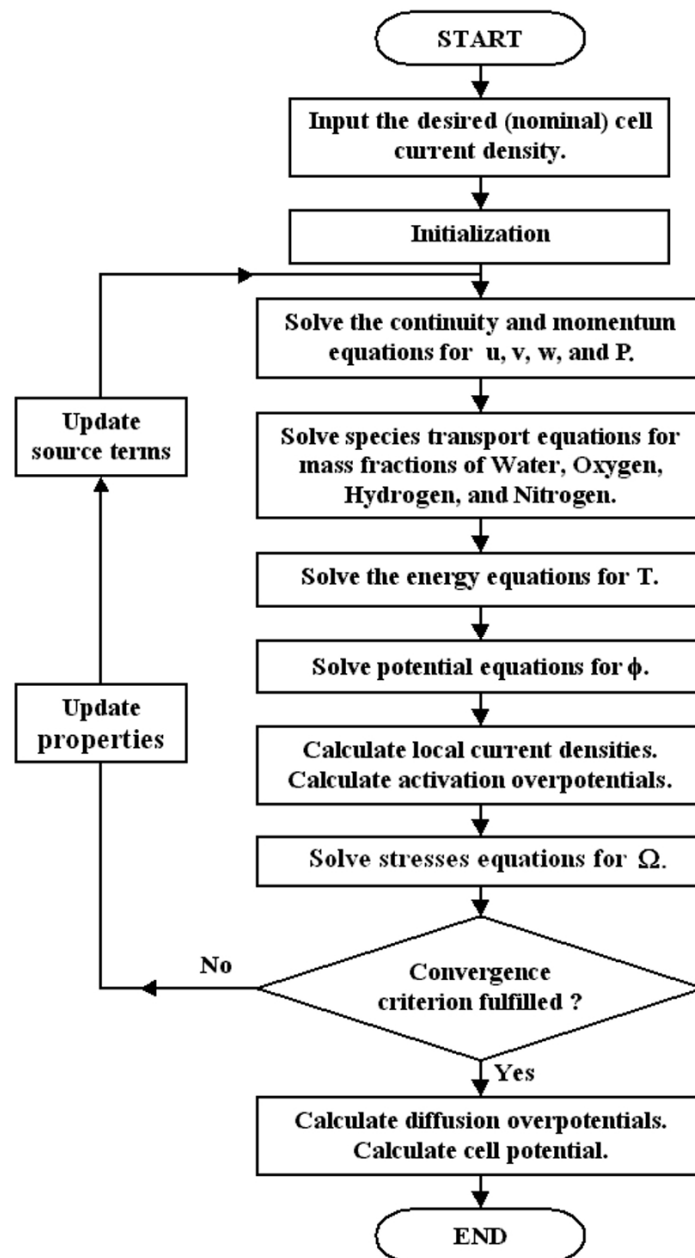


Figure 3. Flow diagram of the solution procedure used

3. Results and discussion

The multi-phase model is validated by comparing model results to experimental data provided by Wang et al. [31]. The importance of phase change to the accurate modelling of fuel cell performance is illustrated. Figure 4 shows the comparison of the polarization curves from the experimental data with the values obtained by the model at different operating fuel cell temperatures. It can be seen that the modelling results compare well with the experimental data. The importance of phase change to the accurate modelling of fuel cell performance is illustrated. Performance curves with and without phase change are also shown in Figure 4 for the base case conditions. Comparison of the two curves demonstrates that the effects of liquid water accumulation become apparent even at relatively low values of current density. Furthermore, when liquid water effects are not included in the model, the cell voltage does not exhibit an increasingly steep drop as the cell approaches its limiting current density. This drop off in performance is clearly demonstrated by experimental data, but cannot be accurately modelled without the incorporation of phase change. By including the effects of phase change, the current model is able to more closely simulate performance, especially in the region where mass transport effects begin to dominate.

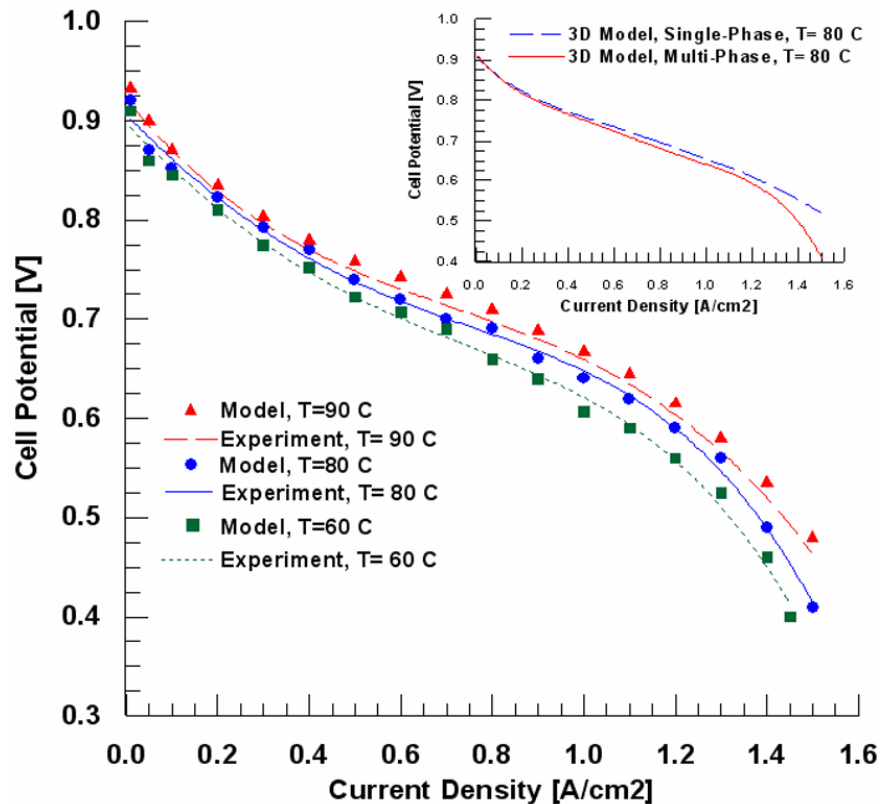


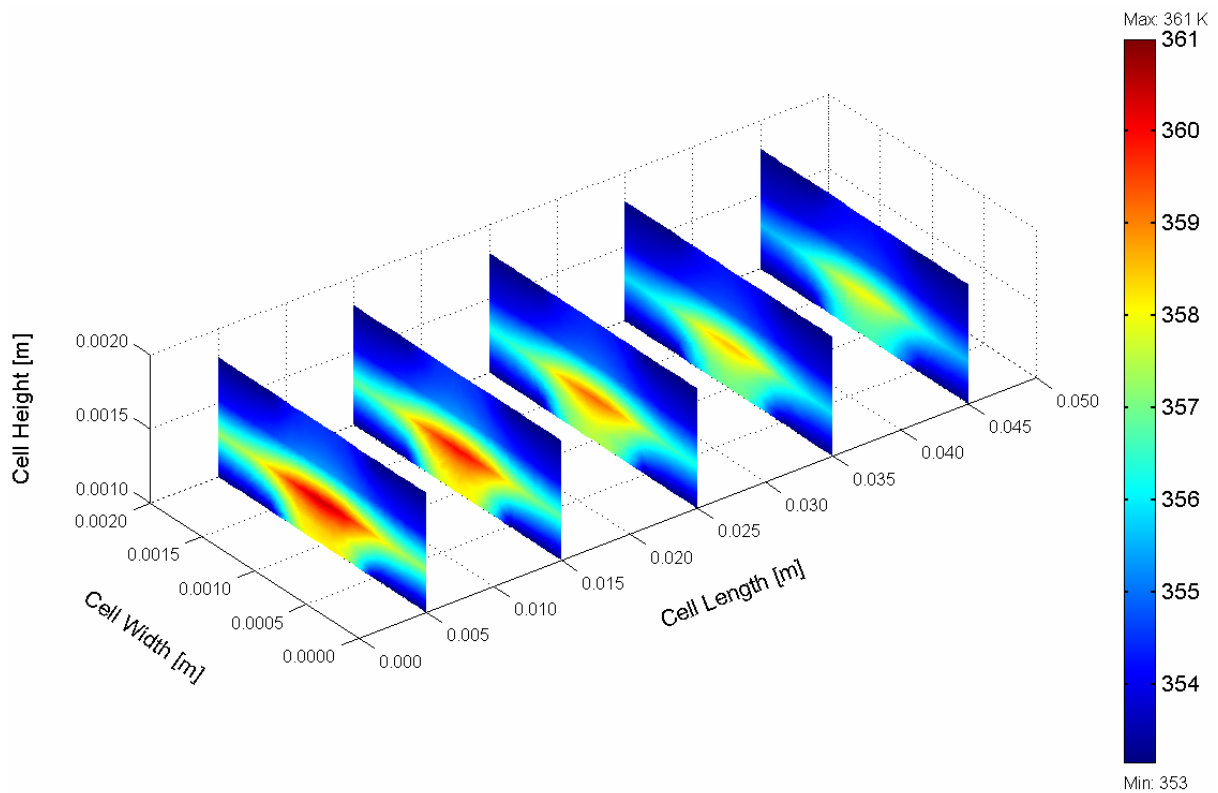
Figure 4. Comparison of the model and the experimental polarization curves

3.1 Base case operating conditions

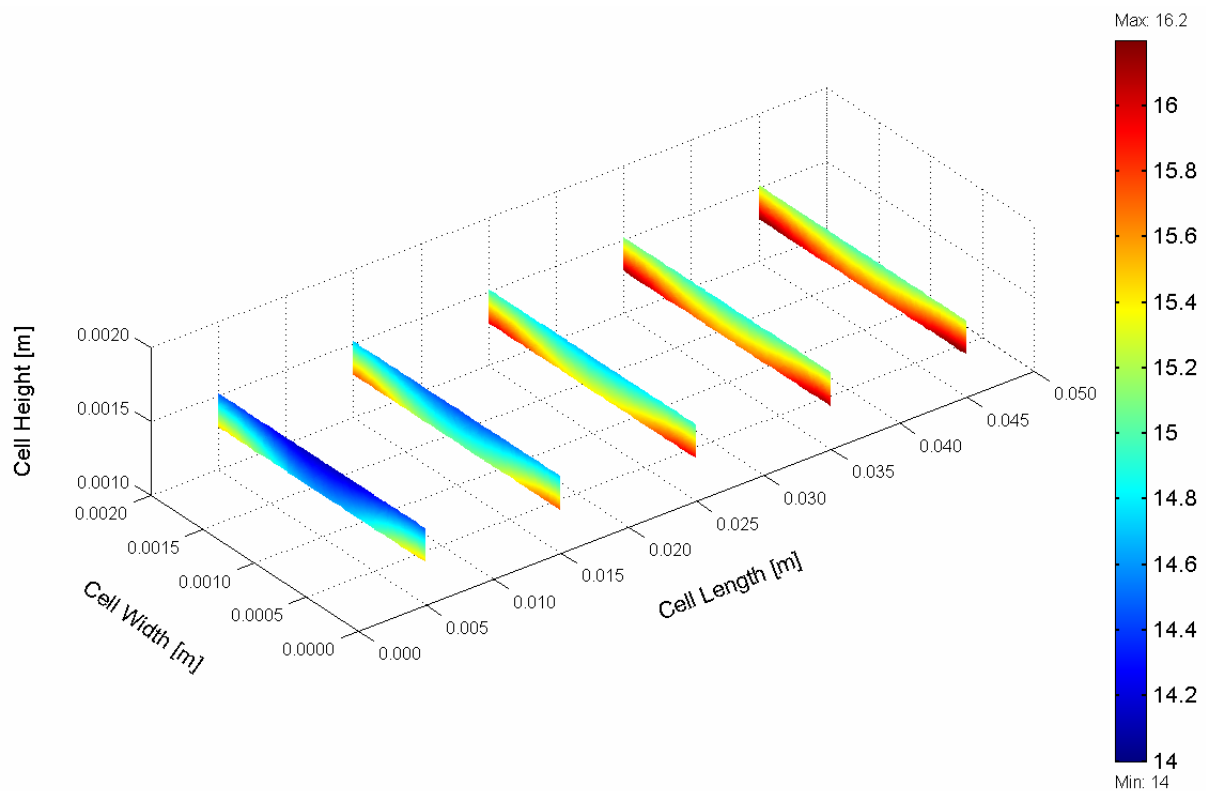
The Membrane-Electrode-Assembly (MEA) is the core component of PEM fuel cell and consists of membrane with the gas-diffusion layers including the catalyst attached to each side. It is influenced by varying local conditions of temperature and humidity. Figure 5a shows the distribution of the temperature inside the MEA during the cell operating at base case condition. In general, the temperature at the cathode side is higher than at the anode side, due to the reversible and irreversible entropy production. Naturally, the maximum temperature occurs, where the electrochemical activity is the highest, which is near the cathode side inlet area. The temperature peak appears in the cathode catalyst layer, implying that major heat generation takes place in this region.

Several transport mechanisms in the cell affect water distribution. In the membrane, primary transport is through (i) electro-osmotic drag associated with the protonic current in the electrolyte, which results in water transport from anode to cathode; and (ii) diffusion associated with water-content gradients in the membrane. One of the main difficulties in managing water in a PEM fuel cell is the conflicting requirements of the membrane and of the catalyst gas diffusion layer. On the cathode side, excessive liquid water may block or flood the pores of the catalyst layer, the gas diffusion layer or even the gas channel, thereby inhibiting or even completely blocking oxygen mass transfer. On the anode side, as water is dragged toward the cathode via electro-osmotic transport, dehumidification of the membrane may occur, resulting in deterioration of protonic conductivity. In the extreme case of complete drying, local burnout of the membrane can result. Figure 5b shows profiles for polymer water content in the membrane for the base case conditions. The influence of electro-osmotic drag and back diffusion are readily apparent from this result.

Due to the varying local conditions of temperature and humidity across the MEA, the hygro and thermal stresses are introduced. Figure 6 shows von Mises stress distribution (contour plots) and deformation shape (scale enlarged 200 times) across the MEA on the y-z plane at $x=10$ mm. The figure illustrates the effect of stresses on the MEA. Because of the different thermal expansion and swelling coefficients between gas diffusion layers and membrane materials with non-uniform temperature distributions in the cell during operation, hygro-thermal stresses and deformation are introduced. The non-uniform distribution of stress, caused by the temperature gradient in the MEA, induces localized bending stresses, which can contribute to delaminating between the membrane and the GDLs.



(a)



(b)

Figure 5. (a) Temperature distribution inside the MEA and (b) water content distribution in the membrane (Base case conditions)

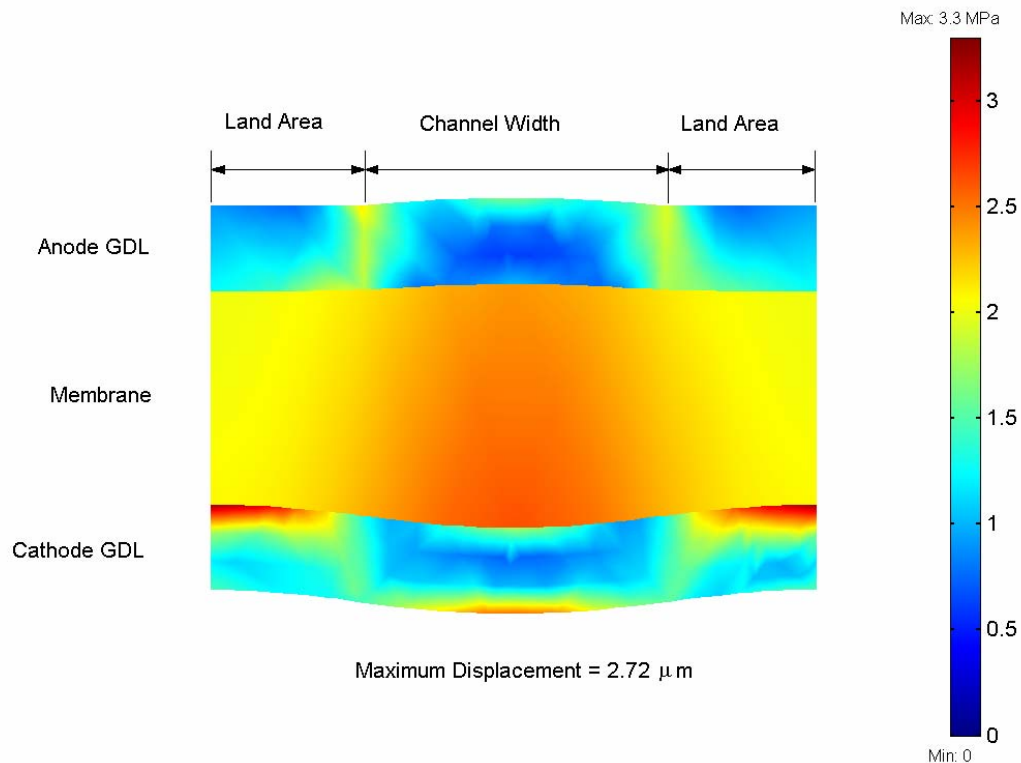


Figure 6. Mises stress distribution (contour) and total displacement (deformed shape plot, X200) in the MEA at base case conditions

3.2 Parametric study

The performance characteristics of the fuel cell based on a certain parameter can be obtained by varying that parameter while keeping all other parameters constant at base case conditions. Results obtained from these parametric studies will allow us to identify the critical parameters for fuel cell performance. Results with different operating conditions for the cell operate at nominal current density of 1.2 A/cm^2 are discussed in the following subsections. In the following subsections only the parameter investigated is changed, all other parameters are at the base case conditions as outlined in Table 1 and Table 2.

3.2.1 Operating parameters

3.2.1.1 Effect of temperature

The temperature basically affects all the different transport phenomena inside the fuel cell. The composition of the incoming gas streams depends strongly on the temperature. Assuming the inlet gases are fully humidified, the partial pressure of water vapour entering the cell depends on the temperature only. Thus, the molar fraction of water vapour is a function of the total inlet pressure and temperature, and so the molar fraction of the incoming hydrogen and oxygen depend on the temperature and pressure as well. At an operating pressure of 1 atm the effect of the temperature on the inlet composition is much stronger than at elevated pressures. At 90 C for atmospheric pressure, almost 68% (molar) of incoming cathode side gas stream consists of water vapour and only around 6.6% is oxygen. The result is a decrease in the molar oxygen fraction at the catalyst layer. It is expected that this will affect mainly the limiting current density. The molar oxygen fraction at the catalyst layer decreases with increasing of the cell operating temperature, due to the reduction of the molar oxygen fraction in the incoming gas streams. The result is a much higher fraction of the local current density and it is generated under the channel area. The results show that the temperature distribution inside the cell show that the maximum temperature occurs at higher cell operating temperature case (90 C), and this leads to increasing the Mises stresses, the total displacement, and the degree of the deformation inside the MEA, but the maximum temperature gradient appears in the lower cell operating temperature case (60 C), due to the high activation overpotential, which leads to more heat generation with drop of the cell voltage. The activation overpotential decreases with increasing of cell operating temperature. This is because of the exchange current density of the oxygen reduction reaction increases rapidly with temperature due to the

enhanced reaction kinetics, which reduces activation losses. A higher temperature leads also to a higher diffusivity of the hydrogen protons in the electrolyte membrane, thereby reducing the membrane resistance and this leads to reducing the potential loss in the membrane. mass transport loss increases as the cell operating temperature increases due to the reduction of the molar oxygen fraction in the incoming gas streams and, hence, a reduction in the molar oxygen fraction at the catalyst layer.

3.2.1.2 Effect of pressure

Similar to the temperature, the operating pressure affects numerous transport parameters that are important for the fuel cell operation. The saturation pressure of water vapour depends only on the temperature and it remains constant for a variation of the inlet pressure. A change in the operating pressure leads to a change in the inlet gas compositions, assuming the inlet gases are fully humidified. The increase in the molar oxygen fraction in the incoming gas streams is significant when the pressure is increased from atmospheric pressure up to 3 atm. A further increase in the pressure from 3 atm to 5 atm does not lead to a significant improvement in terms of the molar oxygen fraction. The effect of the cell operating pressure on the local current distribution shows that the higher cell operating pressure results in more even distribution of the local current density due to the high oxygen concentration at the catalyst layer. This leads to the fact that for a lower cell operating pressure at a constant nominal current density, there is a much stronger distribution of current inside the cell, the maximum local current density being at the inlet under the channel area. Therefore, the maximum temperature gradient appears in the cathode side catalyst layer of the lower cell operating pressure, and this leads to increasing the Mises stresses, the total displacement, and the degree of the deformation inside the MEA. The activation overpotential decreases with increasing of the cell operating pressure. This is because of the exchange current density of the oxygen reduction reaction increases with increasing of the cell operating pressure due to the enhanced reaction kinetics. To reduce mass transport loss, the cathode is usually run at high pressure. In essence, higher pressures help to force the oxygen and hydrogen into contact with the electrolyte and this leads to reducing the mass transport loss.

3.2.1.3 Effect of stoichiometric flow ratio

The stoichiometric flow ratio has an important impact on the water management in the cell. The amount of incoming air determines how much water vapour can be carried out of the cell. The effect of the stoichiometric flow ratio on the local current distribution shows that the higher stoichiometric flow ratio results in more even distribution of the local current density due to the high oxygen concentration at the catalyst layer. Therefore, the maximum temperature gradient appears in the cathode side catalyst layer of the lower stoichiometric flow ratio case, and this leads to increasing the Mises stresses, the total displacement, and the degree of the deformation inside the MEA. For an optimum fuel cell performance, and in order to avoid large temperature gradients inside the fuel cell, it is desirable to achieve a uniform current density distribution inside the cell.

3.2.2 Design parameters

3.2.2.1 Effect of gas channels width

A reduction in the land area width by increasing the width of the gas flow channel enhances the mass transport of the reactions to the catalyst layer that lies under the land area. The result is an increase in the molar oxygen fraction at the catalyst layer with more even distribution. It is expected that this will affect mainly the limiting current density and to a lesser degree, the voltage drop due to mass transport limitations.

The channel width has a large impact on the local current density distribution. For the narrow channel, the local current density can exceed more than 40% of the nominal current density with a sharp drop-off under the land area, where the local current density is about 40% lower than the nominal current density. The wider channel makes for a much more evenly distributed current throughout the cell. However, the temperature peak appears in the cathode side catalyst layer of the wider channel case, implying that major heat generation takes place where the electrochemical activity is the highest, and this leads to increasing the Mises stresses, the total displacement, and the degree of the deformation inside the MEA. This is because of the increase in the width of the gas flow channel means that the velocity of the incoming gas has to be decreased with all remaining parameters remaining constant, and this will decrease the gases velocity in the gas diffusion layer and hence, reduced the convection heat transfer in this region.

Finally, a reduced width of the land area increases the contact resistance between the bipolar plates and the gas diffusion electrodes. Since this is an ohmic loss, it is directly correlated to the land area width.

3.2.2.2 Effect of GDL thickness

The effect of gas diffusion layer thickness on the fuel cell performance is again mostly on the mass transport, as the ohmic losses of the electrons inside the gas diffusion layer are relatively small due to the high conductivity of the carbon fiber paper. A thinner gas diffusion layer increases the mass transport through it, and this leads to reduction the mass transport loss. The molar oxygen fraction at the catalyst layer increases with a decreasing of the gas diffusion layer thickness due to the reduced resistance to the oxygen diffusion by the thinner layer. The distribution of the local current density of the cathode side depends directly on the oxygen concentration. The thicker gas diffusion layer results in more even distribution of the local current density due to the more even distribution of the molar oxygen fraction at the catalyst layer. This leads to the fact that for a thinner gas diffusion layer at a constant current density, there is a much stronger distribution of current inside the cell, the maximum local current density being at the inlet under the channel area.

Therefore, the maximum temperature gradient appears in the cathode side catalyst layer of the thinner gas diffusion layer case, and this leads to increasing the Mises stresses, the total displacement, and the degree of the deformation inside the MEA.

3.2.2.3 Effect of membrane thickness

The effect of membrane thickness on the fuel cell performance is mostly on the resistance of the proton transport across the membrane. The potential loss in the membrane is due to resistance to proton transport across the membrane from anode catalyst layer to cathode catalyst layer. Therefore, a reduction in the membrane thickness means that the path travelled by the protons will be decreased, thereby reducing the membrane resistance and this leads to reducing the potential loss in the membrane, which in turn leads to less heat generation in the membrane, and this leads to reducing the Mises stresses, the total displacement, and the degree of the deformation inside the MEA.

These results suggested that reducing the membrane thickness played a significant role in promoting cell performance. However, there is a limitation to this reduction, due to the effect of increased gas cross-over with very thin membranes.

3.2.3 Material parameters

3.2.3.1 Effect of GDL porosity

The porosity of the gas diffusion layer has two comparing effects on the fuel cell performance; as the porous region provides the space for the reactants to diffuse towards the catalyst region, an increase in the porosity means that the onset of mass transport limitations occurs at higher current densities, i.e. it leads to higher limiting currents.

The adverse effect of a high porosity is increase in the contact resistance. Higher gas diffusion layer porosity improves the mass transport within the cell and this leads to reducing the mass transport loss. The molar oxygen fraction at the catalyst layer increases with more even distribution with an increasing in the porosity. This is because of a higher value of the porosity provides less resistance for the oxygen to reach the catalyst layer. A higher porosity evens out the local current density distribution. For a lower value of the porosity a much higher fraction of the total current is generated under the channel area. This can lead to local hot spots inside the membrane electrode assembly. These hot spots can lead to a further drying out of the membrane, thus increasing the electric resistance, which in turn leads to more heat generation and therefore increasing the Mises stresses, the total displacement, and the degree of the deformation inside the MEA.

Thus, it is important to keep the current density relatively even throughout the cell. As mentioned above, another loss mechanism that is important when considering different gas diffusion layer porosities is the contact resistance. Contact resistance occurs at all interfaces inside the fuel cell. The magnitude of the contact resistance depends on various parameters such as the surface material and treatment and the applied stack pressure. The electrode porosity has a negative effect on electron conduction, since the solid matrix of the gas diffusion layer provide the pathways for electron transport, the higher volume porosity increases resistance to electron transport in the gas diffusion layers.

3.2.3.2 Effect of GDL thermal conductivity

Thermal management is required to remove the heat produced by the electrochemical reaction in order to prevent drying out of the membrane and excessive thermal stresses that may result in rupture of the membrane. The small temperature differential between the fuel cell stack and the operating environment make thermal management a challenging problem in PEM fuel cells. The maximum temperature with higher gradient appears in the cathode side catalyst layer of the lower thermal conductivity. Heat generated in the catalyst layer is primarily removed through the gas diffusion layer to the current collector rib by lateral conduction. This process is controlled by the gas diffusion later thermal conductivity. Therefore, the membrane temperature is strongly influenced by the gas diffusion layer thermal conductivity, indicating a significant role played by lateral heat conduction through the gas diffusion layer in the removal of waste heat to the ambient. Therefore, a gas diffusion layer material having higher thermal conductivity is strongly recommended for fuel cells designed to operate with high power.

3.2.3.3 Effect of membrane thermal conductivity

The higher membrane conductivity results in more even distribution of the temperature inside the cell. The lower membrane conductivity means that it is likely that heat accumulates at the cathode catalyst surface during operation. Therefore, a membrane material having higher thermal conductivity is strongly recommended for fuel cells designed to operate with high power density.

3.3 Optimal conditions to achieve long cell life

Results with deferent operating conditions are summarized in Figure 7. The maximum displacement at various operating conditions is compared at constant nominal current density of 1.2 A/cm^2 . To achieve long cell life, the results show that the cell must be operate at lower cell operating temperature, higher cell operating pressure, higher stoichiometric flow ratio, and must have higher GDL porosity, higher GDL thermal conductivity, higher membrane thermal conductivity, narrower gases channels, thicker gas diffusion layers, and thinner membrane.

The parameters that achieve long cell life are presented in Table 3. These parameters have been used in the CFD model to predict the stresses, displacement, and the degree of deformation in the cell for the optimal conditions. Figure 8 shows von Mises stress distribution (contour plots) and deformation shape (scale enlarged 200 times) for MEA on the y-z plane at $x=10 \text{ mm}$ for optimal operating conditions of long cell life (Table 3). The figure illustrates the effect of stresses on the MEA. This distribution of stresses is more uniform with less important displacement compared with all previous parametric results. The results show that the maximum displacement is only 1.37 micro m. This value is less than the displacement that occurs in the base case operating conditions by about 50%.

Table 3. Optimal parameters for optimum design and operating conditions to achieve long cell life

| Parameter | Value |
|----------------------------------------------------------------------------------------------------------------------------------|-----------|
| Cell operating temperature | 60 C |
| Cell operating pressure | 5 atm |
| Stoichiometric flow ratio | 3 |
| Gas channel width | 0.8 mm |
| GDL porosity | 0.5 |
| GDL thickness | 0.3 mm |
| GDL thermal conductivity | 2.9 W/m.K |
| Membrane thermal conductivity | 0.6 W/m.K |
| Membrane thickness | 0.2 mm |
| <ul style="list-style-type: none"> All other parameters keeping constant at base case conditions. (Table 1 and 2) | |

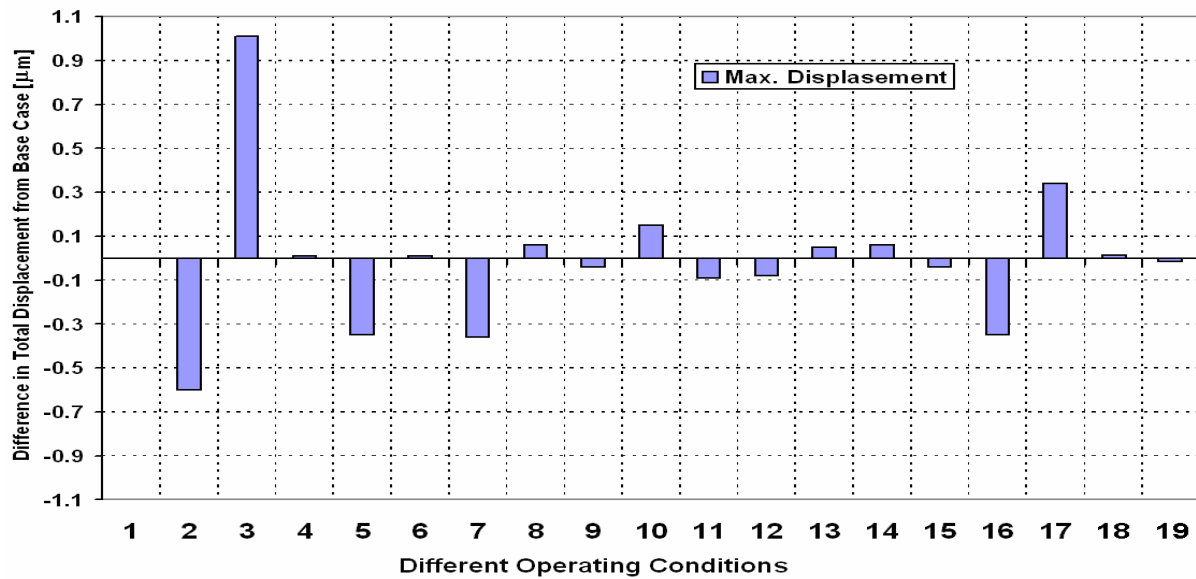


Figure 7. Change in maximum displacement with different operating conditions compared to the base case conditions

Key:

- 1- Base case
- 2- Cell operating temperature = 60 C
- 3- Cell operating temperature = 90 C
- 4- Cell operating pressure = 1 atm
- 5- Cell operating pressure = 5 atm
- 6- Stoichiometric flow ratio = 1.5
- 7- Stoichiometric flow ratio = 3
- 8- GDL porosity = 0.3
- 9- GDL porosity = 0.5

- 10- GDL thermal conductivity = 0.5 W/m.K
- 11- GDL thermal conductivity = 2.9 W/m.K
- 12- Gas channel width = 0.8 mm
- 13- Gas channel width = 1.2 mm
- 14- GDL thickness = 0.2 mm
- 15- GDL thickness = 0.3 mm
- 16- Membrane thickness = 0.2 mm
- 17- Membrane thickness = 0.26 mm
- 18- Membrane thermal conductivity = 0.3 W/m.K
- 19- Membrane thermal conductivity = 0.6 W/m.K

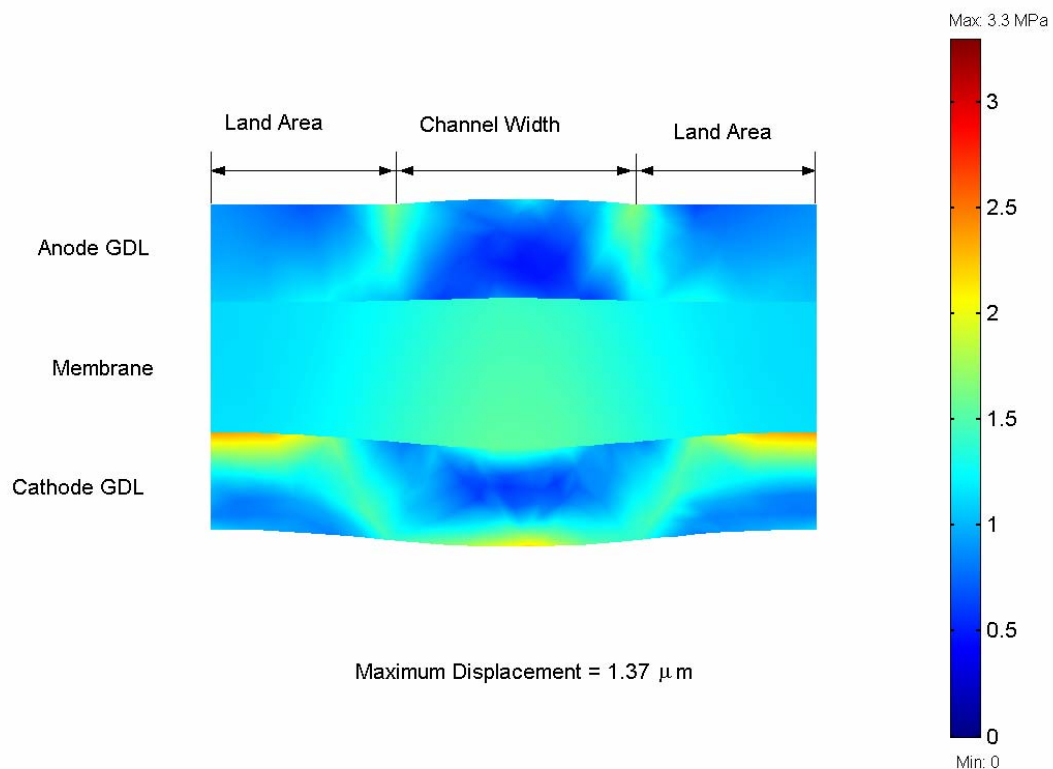


Figure 8. Mises stress distribution (contour) and total displacement (deformed shape plot, X200) in the MEA for optimum design and operating conditions (Table 3)

4. Conclusion

A full three-dimensional, multi-phase computational fluid dynamics model of a PEM fuel cell has been developed to investigate the hygro-thermal stresses in PEM fuel cell, which developed during the cell operation due to the changes of temperature and relative humidity. A unique feature of the present model is to incorporate the effect of hygro and thermal stresses into actual three-dimensional fuel cell model. The behaviour of the gas diffusion layers and membrane during operation of a unit cell has been studied and investigated under real cell operating conditions. The results show that the non-uniform distribution of stresses, caused by the temperature gradient in the cell, induces localized bending stresses, which can contribute to delaminating between the membrane and the gas diffusion layers. These stresses may explain the occurrence of cracks and pinholes in the membrane under steady-state loading during regular cell operation. Parametric and optimization study using this model has been performed. The study quantifies the impact of operating, design, and material parameters on fuel cell performance. The model is shown to be able to: (1) understand the many interacting, complex electrochemical and transport phenomena that cannot be studied experimentally; (2) identify limiting steps and components; and (3) provide a computer-aided tool for design and optimization of future fuel cell with much higher power density, long cell life, and lower cost. To achieve long cell life, the results show that the cell must be operate at lower cell operating temperature, higher cell operating pressure, higher stoichiometric flow ratio, and must have higher GDL porosity, higher GDL thermal conductivity, higher membrane thermal conductivity, narrower gases channels, thicker gas diffusion layers, and thinner membrane.

In conclusion, the development of physically representative models that allow reliable simulation of the processes under realistic conditions is essential to the development and optimization of fuel cells, improve long-term performance and lifetime, the introduction of cheaper materials and fabrication techniques, and the design and development of novel architectures.

References

- [1] Zhang, S.; Yuan, X.; Wang, H.; Merida, W.; Zhu, H.; Shen, J.; Wu, S.; Zhang, J. A review of accelerated stress tests of MEA durability in PEM fuel cells. *Int. J. Hydrogen Energy*, 2009; 34(1): 388-404.
- [2] Wu, J.; Yuan, X.Z.; Martin, J.J.; Wang, H.; Zhang, J.; Shen, J.; Wu, S.; Merida, W. A review of PEM fuel cell durability: Degradation mechanisms and mitigation strategies. *J. Power Sources*, 2008; 184(1): 104-119.
- [3] Beuscher, U.; Cleghorn, S.J.C.; Johnson, W.B. Challenges for PEM fuel cell membranes. *Int J Energy Res* 2005; 29(12): 1103-1112.
- [4] Gode, P.; Ihonen, J.; Strandroth, A.; Ericson, H.; Lindbergh, G.; Paronen, M.; Sundholm, F.; Sundholm, G.; Walsby, N. Membrane durability in a pem fuel cell studied using PVDF based radiation grafted membranes fuel cells. *Fuel Cells* 2003; 3(1-2): 21-27.
- [5] Crum, M.; Liu, W. Effective Testing Matrix for Studying Membrane Durability in PEM Fuel Cells. Part 2. Mechanical Durability and Combined Mechanical and Chemical Durability, vol. 3. Electrochemical Society Inc., Pennington, NJ 08534-2896, United States, Cancun, Mexico, 2006: 541-550.
- [6] Marrony, M.; Barrera, R.; Quenet, S.; Ginocchio, S.; Montelatici, L.; Aslanides, A. Durability study and lifetime prediction of baseline proton exchange membrane fuel cell under severe operating conditions. *J. Power Sources*, 2008; 182(2): 469-475.
- [7] Stanic V, Hoberech M. Mechanism of pin-hole formation in membrane electrode assemblies for PEM fuel cells. *Electrode Assemblies for PEM Fuel Cells*, Electrochemical Society Inc., Pennington, NJ 08534-2896, United States, Honolulu, HI, United States, 2004; p. 1891.
- [8] Ramaswamy, N.; Hakim, N.; Mukerjee, S. Degradation mechanism study of perfluorinated proton exchange membrane under fuel cell operating conditions. *Electrochimica Acta* 2008; 53(8): 3279-3295.
- [9] Tang Y, Karlsson AM, Santare MH, Gilbert M, Cleghorn S, Johnson WB. An experimental investigation of humidity and temperature effects on the mechanical properties of perfluorosulfonic acid membrane. *J Mater Sci Eng* 2006; 425(1-2): 297-304.
- [10] Xie J, Wood DL, Wayne DM, Zawodzinski T, Borup RL. Durability of polymer electrolyte fuel cells at high humidity conditions. *J Electrochem Soc* 2005; 152(1): A104-A113.
- [11] Kim, S.; Mench, M.M. Investigation of temperature-driven water transport in polymer electrolyte fuel cell: phase-change-induced flow. *J Electrochem Soc* 2009; 156(3): B353-B362.

- [12] Kim, S.; Mench, M.M. Investigation of temperature-driven water transport in polymer electrolyte fuel cell: Thermo-osmosis in membranes. *J. Membrane Sci.* 2009; 328(1-2): 113-120.
- [13] Berning, T.; Lu, D.M.; Djilali, N. Three-dimensional computational analysis of transport phenomena in a PEM fuel cell. *J. Power Sources*, 2002; 106(1-2): 284-294.
- [14] Berning, T.; Djilali, N. Three-dimensional computational analysis of transport phenomenon in a PEM fuel cell-a parametric study. *J. Power Sources*, 2003; 124(2): 440-452.
- [15] Sivertsen, B.R.; Djilali, N. CFD based modelling of proton exchange membrane fuel cells. *J. Power Sources*, 2005; 141(1): 65-78.
- [16] Webber, A.; Newman, J.A. Theoretical study of membrane constraint in polymer-electrolyte fuel cell. *AIChE J.*, 2004; 50(12): 3215-3226.
- [17] Tang, Y.; Santare, M.H.; Karlsson, A.M.; Cleghorn, S.; Johnson, W.B. Stresses in proton exchange membranes due to hygro-thermal loading. *J. Fuel Cell Sci.&Tech. ASME*, 2006; 3(5): 119-124.
- [18] Kusoglu, A.; Karlsson, A.M.; Santare, M.H.; Cleghorn, S.; Johnson, W.B. Mechanical response of fuel cell membranes subjected to a hygro-thermal cycle. *J. Power Sources*, 2006; 161(2): 987-996.
- [19] Kusoglu, A.; Karlsson, A.M.; Santare, M.H.; Cleghorn, S.; Johnson, W.B. Mechanical behavior of fuel cell membranes under humidity cycles and effect of swelling anisotropy on the fatigue stresses. *J. Power Sources*, 2007; 170(2): 345-358.
- [20] Solasi, R.; Zou, Y.; Huang, X.; Reifsnider, K.; Condit, D. On mechanical behavior and in-plane modeling of constrained PEM fuel cell membranes subjected to hydration and temperature cycles. *J. Power Sources*, 2007; 167(2): 366-377.
- [21] Bograchev, D.; Gueguen, M.; Grandidier, J-C.; Martemianov, S. Stress and plastic deformation of MEA in fuel cells stresses generated during cell assembly. *J. Power Sources*, 2008; 180(2): 393-401.
- [22] Suvorov, A.P.; Elter, J.; Staudt, R.; Hamm, R.; Tudryn, G.J.; Schadler, L.; Eisman, G. Stress relaxation of PBI based membrane electrode assemblies. *Int. J. Solids and Structures*, 2008; 45(24): 5987-6000.
- [23] Tang, Y.; Kusoglu, A.; Karlsson, A.M.; Santare, M.H.; Cleghorn, S.; Johnson, W.B. Mechanical properties of a reinforced composite polymer electrolyte membrane and its simulated performance in PEM fuel cells. *J. Power Sources*, 2008; 175(2): 817-825.
- [24] Bograchev, D.; Gueguen, M.; Grandidier, J-C.; Martemianov, S. Stress and plastic deformation of MEA in running fuel cell. *Int. J. Hydrogen Energy*, 2008; 33(20): 5703-5717.
- [25] Al-Baghdadi, MARS.; Shahad, H. Effect of operating parameters on the hygro-thermal stresses in proton exchange membranes of fuel cells. *Int. J. Hydrogen Energy*, 2007; 32(17): 4510-4522.
- [26] Fuller, E.N.; Schettler, P.D.; Giddings, J.C. A new method for prediction of binary gas-phase diffusion coefficients. *Ind. Eng. Chem.*, 1966; 58(5): 18-27.
- [27] Berning, T.; Djilali, N. A 3D, multi-phase, multicomponent model of the cathode and anode of a PEM fuel cell. *J. Electrochem. Soc.*, 2003; 150(12): A1589-A1598.
- [28] Nguyen, P.T.; Berning, T.; Djilali, N. Computational model of a PEM fuel cell with serpentine gas flow channels. *J. Power Sources*, 2004; 130(1-2): 149-157.
- [29] Al-Baghdadi, MARS.; Shahad, H. Optimization study of a PEM fuel cell performance using 3D multi-phase computational fluid dynamics model. *Journal of Zhejiang University SCIENCE-A* 2007; 8(2): 285-300.
- [30] Lampinen, M.J.; Fomino, M. Analysis of free energy and entropy changes for half-cell reactions. *J. Electrochem. Soc.*, 1993; 140(12): 3537-3546.
- [31] Wang, L.; Husar, A.; Zhou, T.; Liu, H. A parametric study of PEM fuel cell performances. *Int. J. Hydrogen Energy*, 2003; 28(11): 1263-1272.
- [32] Parthasarathy, A.; Srinivasan, S.; Appleby, J.A.; Martin, C.R. Pressure dependence of the oxygen reduction reaction at the platinum microelectrode/nafeon interface: electrode kinetics and mass transport. *J. Electrochem. Soc.*, 1992; 139(10): 2856-2862.
- [33] Siegel, N.P.; Ellis, M.W.; Nelson, D.J.; von Spakovsky M.R. A two-dimensional computational model of a PEMFC with liquid water transport. *J. Power Sources*, 2004; 128(2): 173-184.
- [34] Hu, M.; Gu A.; Wang, M.; Zhu, X.; Yu, L. Three dimensional, two phase flow mathematical model for PEM fuel cell. Part I. Model development. *Energy Conversion Manage*, 2004; 45(11-12): 1861-1882.

- [35] Product Information, DuPont™ Nafion® PFSA Membranes N-112, NE-1135, N-115, N-117, NE-1110 Perfluorosulfonic Acid Polymer. NAE101, 2005.